Memory and Transduction Prospects for Silicon *T* Center Devices

Daniel B. Higginbottom,[1,2] Faezeh Kimiaee Asadi,[3] Camille Chartrand,[1,2] Jia-Wei Ji,[3] Laurent Bergeron,[1,2] Michael L.W. Thewalt,[1] Christoph Simon,[3] and Stephanie Simmons[1,2,*]

[1] *Department of Physics, Simon Fraser University, Burnaby, British Columbia V5A 1S6, Canada*

[2] *Photonic Inc., Coquitlam, British Columbia V3K 6T1, Canada*

[3] *Department of Physics & Astronomy, Institute for Quantum Science and Technology, University of Calgary, 2500 University Drive NW, Calgary, Alberta T2N 1N4, Canada*

(Received 13 September 2022; accepted 13 March 2023; published 17 April 2023)

The *T* center, a silicon-native spin-photon interface with telecommunication-band optical transitions and long-lived microwave qubits, offers an appealing new platform for both optical quantum memory and microwave-to-optical telecommunication-band transduction. A wide range of quantum memory and transduction schemes could be implemented with*T* center ensembles with sufficient optical depth, with advantages and disadvantages that depend sensitively on the ensemble properties. In this work we characterize *T* center spin ensembles to inform device design. We perform the first *T* ensemble optical depth measurement and calculate the improvement in center density or resonant optical enhancement required for efficient optical quantum memory. We further demonstrate a coherent microwave interface by coherent population trapping and Autler-Townes splitting. We then determine the most promising microwave and optical quantum memory protocol for such ensembles. By estimating the memory efficiency both in free space and in the presence of a cavity, we show that efficient optical memory is possible with reasonable optical density forecasts. Finally, we formulate a transduction proposal and discuss the achievable efficiency and fidelity.

DOI: 10.1103/PRXQuantum.4.020308

I. INTRODUCTION

Quantum memories and transducers are enabling technologies for the global quantum internet. Optical quantum memories that coherently store and recall unknown states of a traveling optical field on demand [1] are a component of quantum repeaters [2–5] to increase the entanglement distribution range, and therefore the secure communication range, of quantum networks [6] as well as a means of synchronizing processes with optical quantum computers. Microwave (MW) quantum memories, on the other hand, can interface with microwave frequency material qubits, including superconducting circuit qubits—arguably the most advanced quantum computing platform at present—to extend circuit depth and reduce no-operation error rates [7].

Long-coherence spin ensembles have been proposed as quantum memories for both applications, with considerable research into optical quantum memories in particular. To date, several quantum memory protocols, including electromagnetically induced transparency (EIT) [8], atomic frequency comb [9,10], controlled reversible inhomogeneous broadening [11], and Autler-Townes (AT) splitting (ATS) [12], based on platforms such as rare-earth ions [10,13], nitrogen-vacancy centers in diamond [14], atomic vapors [15,16], and Bose-Einstein condensates [17,18] have been proposed. However, few of these systems operate in a telecommunications band. Extending the quantum internet to a global scale requires optical quantum memories compatible with satellite communications as well as terrestrial optical fiber networks.

Similarly, efficient and coherent conversion between gigahertz microwave signals and terahertz optical signals is essential for networking microwave material qubits [19]. Transduction from microwave to telecom photons could enable, for example, networking of superconducting quantum processors and spin quantum processors [20,21] via the global quantum internet. There are several remarkable experimental demonstrations [22–25] of as well as theoretical approaches [26–29] for reversible conversion between microwave and optical fields. In general, quantum transduction can be achieved through intermediate systems such as atomic ensembles [22,25,28,30], electro-optical

*s.simmons@sfu.ca

systems [24,31], electro-optomechanical systems [23,32], and other systems including molecules and ferromagnets [33,34].

Ensembles of atoms or atomlike systems combining long-coherence microwave spin qubits and optical transitions are therefore a versatile "Swiss-army knife" platform suitable for microwave and optical memory as well as microwave-to-optical transduction. Identifying and developing long-coherence quantum systems combining narrow and absorptive microwave and telecom optical transitions is an important milestone for designing a quantum network. However, to date few suitable systems have been identified. Memory and transduction proposals of this kind have focused almost exclusively on Er^{3+}, which combines narrow MW and telecom optical transitions in many crystal hosts [26,28,30]. Although the optical transition is comparatively weak, significant optical depths have been observed with concentrated Er^{3+} ensembles in large crystals [35].

The newly rediscovered silicon T center offers native O-band telecom access and long-lived spins operating at microwave frequencies [36,37]. Notably, silicon is an attractive host material for such a system, as it is already the substrate of choice for a wide variety of quantum platforms, including ion traps [38], quantum dots [39], superconducting qubits [40], and, naturally, impurity and defect spins in silicon [41] and silicon photonics [42]. The T center integrates with silicon photonic devices on CMOS-compatible wafers as a waveguide and fiber-networked quantum information platform [37] that could further mediate between other silicon quantum technologies packaged on-chip, such as superconducting, trapped ion, and gate-defined quantum dot qubits, for a complete, all-silicon hybrid quantum information platform.

In this paper we introduce the prospects of T centers for microwave quantum memory, optical quantum memory, and microwave-to-optical quantum transducers. We first briefly review the known properties of the T center as revealed by recent studies. Then, we further characterize T center ensembles experimentally toward the goal of quantum memories and transducers. We report measurements of T center optical depth (OD) in Sec. III, microwave coherent population trapping (CPT) in Sec. IV, and microwave ATS in Sec. V. Informed by these measurements, in Sec. VI, we estimate the efficiency of applicable optical memory schemes, including EIT and ATS. In Sec. VII we propose placing the ATS memory in a cavity and present a model of this configuration to derive the resonator requirements for efficient T center microwave quantum memories. On the basis of these results, we then consider the potential of combining the optical and microwave ATS schemes to design a transduction protocol in Sec. VIII. Finally, we conclude with future directions in Sec. IX. A notation key is provided (Appendix C) to keep track of the important properties and variables for each of these applications.

II. THE *T* CENTER

The T center is a luminescent silicon defect with a sharp emission line at 935 meV, in the telecom O band. Early work [43,44] established that T centers comprise two nonequivalent carbon atoms and a hydrogen atom. Some of the T center parameters required to calculate quantum memory and transduction efficiencies, including the level structure, optical linewidths and lifetimes, and spin coherence times, were established recently [36,37,45,46]. The remaining key parameters—optical depth, microwave coupling strengths and two-photon microwave linewidth—are obtained in this work and used in proof-of-principle quantum memory precursor experiments.

Spectroscopy of T center ensembles [36] established that the ground state has a tightly bound $s = 1/2$ electron coupled to the hydrogen nuclear $s = 1/2$ spin through an anisotropic hyperfine interaction. In its optically excited state, a bound exciton is formed, the electron spins form a singlet state, and there remains an unpaired $s = 3/2$ hole. The fourfold degeneracy of free holes in silicon is lifted in the reduced symmetry of the T center to form two distinct excited state doublets labeled "TX_0" and "TX_1" separated by 1.76 meV. Thermal excitation between these two states is negligible below approximately 2 K. Studies of TX_0 with ensembles and single centers revealed remarkable optical linewidths sufficient to resolve the ground state electron spin splitting at low fields [36,37].

The TX_0 lifetime τ is 0.94 μs in bulk silicon [36]. The radiative efficiency, η_R, of this transition is not precisely known. To date, measurements with bulk ensembles have not found evidence of nonradiative relaxation [36]. First-principles theoretical calculations indicate $0.19 < \eta_R < 0.72$ [47], and single-center photon fluorescence rates bound $\eta_R \geq 0.03$ [37]. The zero-phonon (ZP) fraction (η_{ZP}), or Debye-Waller factor, is known to be 0.23 [36].

The schematic level structure in Fig. 1 shows TX_0 under an applied magnetic field, with four resolved optical transitions, A–D, between the ground state electron and excited state hole states. The T center has 24 possible orientations, forming 12 inequivalent inversion symmetry subsets i, each with its own set of optical transitions, A_i–D_i, determined by the effective anisotropic hole Landé factor $0.85 < g_{Hi} < 3.5$ for a particular magnetic field orientation. Optically detected magnetic resonances (ODMRs) reveal ground state hyperfine splitting under microwave or radio-frequency (rf) excitation. Both the "allowed" nuclear-spin-preserving microwave transitions, $MW_{\Uparrow}$ and $MW_{\Downarrow}$, and the "forbidden" microwave transitions, X_m and X_p, are observed to be strong. The T center therefore boasts both optical and microwave Λ and V transitions for interfacing between traveling fields and spins. The nuclear spin states of the hydrogen nucleus become optically accessible when homogeneous linewidths are sufficiently narrow [46].

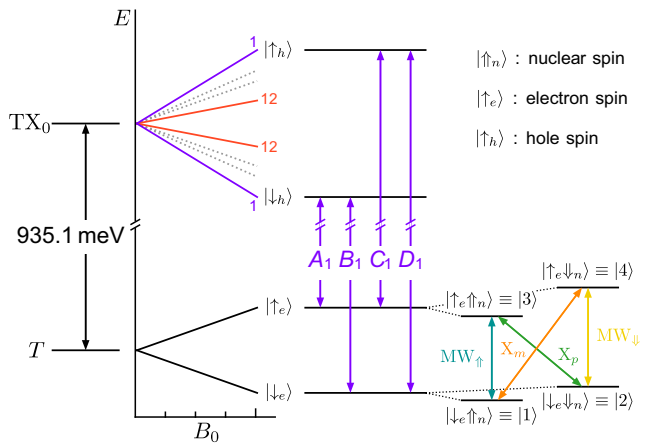

FIG. 1. Energy level diagram of the T center 935.1-meV TX_0 optical transition. Under a magnetic field, the unpaired electron spin of the paramagnetic ground state T and the unpaired hole spin of the excitonic excited state TX_0 split into doublets. The anisotropic hole spin determines 12 orientational subsets for a given magnetic field orientation, with optical transitions A_i–D_i for subset i, that may be optically resolved. The nuclear spin transitions are resolvable with microwave addressing.

Isotopically purified ^{28}Si improves on both the spin properties and the optical properties of the T center. Removal of ^{29}Si atoms (spin-1/2 nuclei) reduces the magnetic noise bath and increases native spin coherence times. Removal of mass variations due to both ^{29}Si and ^{30}Si dramatically reduces the optical inhomogeneous broadening, Γ^{in}. Ensemble optical inhomogeneous linewidths $\Gamma^{\text{in}}/2\pi$ as low as 33 MHz have been observed in ^{28}Si T center ensembles [36]. Hahn echo measurements in ^{28}Si crystals revealed electron and nuclear spin coherence times (T_2^e and T_2^n) of 2.1 ms and 1.1 s, respectively [36]. Both T center spins offer a memory advantage compared with superconducting qubits, and the nuclear spin coherence time is sufficient for repeaters in terrestrial quantum networks. Measurements of spectral diffusion, Γ^{SD}, have indicated that the ^{28}Si ensemble optical linewidths may be close to diffusion limited, $\Gamma^{\text{SD}}/2\pi = 27(12)$ MHz, and that spectral diffusion remains low in natural silicon samples even as the inhomogeneous linewidth increases to 6 GHz [45]. Measurements of the "instantaneous" homogeneous linewidth, Γ^{hom}, have shown that T emission in ^{28}Si can be almost lifetime limited ($\Gamma^{\text{hom}}/2\pi = 690$ kHz $\sim 4 \times 1/2\pi\tau$), and increases to approximately 11 MHz in silicon-on-insulator (SOI) ensembles measured to date [46].

In the following sections we extend these studies by characterizing the optical absorption properties of ^{28}Si T center ensembles to determine the requirements for T center optical quantum memories. We further implement the first coherent Λ and V schemes for T centers as a precursor to quantum memory and transduction protocols.

III. OPTICAL DEPTH

An efficient quantum memory fundamentally requires signal absorption approaching 100% for the reversible transfer of information. The precise OD requirement depends on the choice of memory scheme (which we discuss in Sec. VI), but an OD $d > 5$ is a starting point for practical memories. Here we report the first optical absorption measurements of T centers and extrapolate what ODs are feasible in the near term for T center quantum memories. An approximately-5-mm-thick ^{28}Si sample is electron irradiated and annealed according to the procedure in Appendix B to produce a significant concentration of T centers. We measure the complete photoluminescence (PL) spectrum under above-band excitation by Fourier transform infrared (FTIR) spectroscopy; see Fig. 2(a). Details regarding the prominent TX_0 zero-phonon line (ZPL) are shown in Fig. 2(b). In addition to the PL spectrum (blue), we resolve the ZPL by photoluminescence excitation (PLE) spectroscopy, resonantly exciting TX_0 with a scanning laser and detecting fluorescence from the phonon sideband to determine an ensemble ZPL linewidth

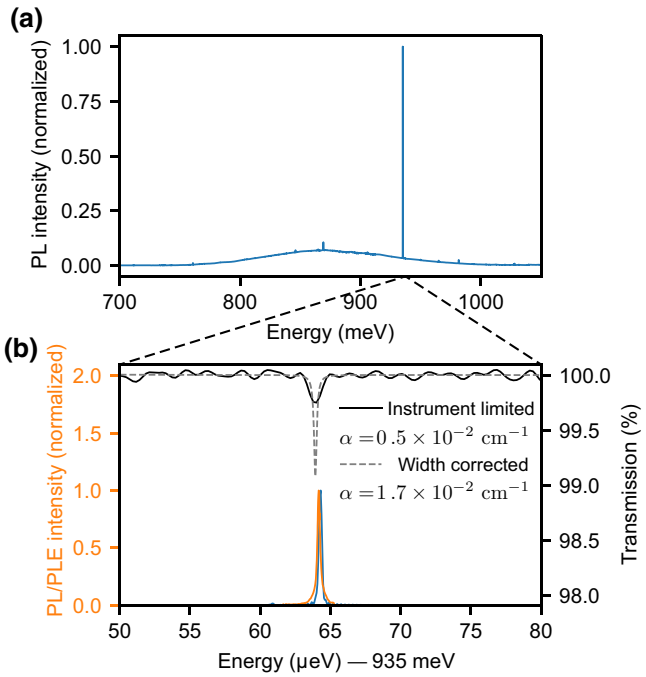

FIG. 2. (a) PL spectrum of a T center ensemble in ^{28}Si. (b) High-resolution PL spectrum about the TX_0 zero-phonon peak (blue) and PLE spectrum of the same sample (orange). The corresponding absorption spectrum (black) is instrument resolution limited. We calculate an area-preserving corrected absorption spectrum (dashed black line) with linewidth and shape matched to the PLE spectrum.

$\Gamma^{\text{in}}/2\pi$ of 56 MHz (orange). This linewidth is an inhomogeneous factor of 331 times the lifetime-limited linewidth, and is slightly larger than the smallest linewidth measured [36]. The corresponding FTIR optical transmission spectrum (black), taken with a continuum light source and a sample temperature of 1.4 K, is presented on a separate axis in Fig. 2(b). Absorption at the T center ZPL is evident with peak absorption of 0.27(1)%, limited by the instrument resolution. Assuming the true absorption linewidth is identical to the PL linewidth, we infer a corrected peak absorption of 0.93(3)%, corresponding to peak resonant OD $d_{\text{corr}} = 0.009$ and resonant absorption coefficient $\alpha_{\text{corr}} = 0.017/\text{cm}$.

This first absorption measurement allows us to assess the feasibility of T center ensembles in the OD regime required for optical quantum memories. A considerable increase in optical depth over the sample measured here is required to operate an efficient quantum memory, but recent measurements indicate that orders of magnitude improvements are possible. First, we can compare the concentration of this sample with theoretical limits and concentrations observed in other work. The T center concentration c_T can be determined from the integrated absorption line area $\int \alpha dV$ shown in Fig. 2 [48]:

$$c_T = \frac{g_1}{g_2}\frac{8\pi n^2 \tau_{\text{ZP}} \int \alpha dV}{h\lambda^2}, \tag{1}$$

where g_1 and g_2 are the degeneracy of the ground state and the degeneracy of the excited state, $n = 3.45$ is the silicon index of refraction at cryogenic temperatures, $\tau_{\text{ZP}} = \tau/\eta_R\eta_{\text{ZP}}$ is the ZP radiative lifetime, h is Planck's constant, and $\lambda = 1326$ nm is the wavelength.

Assuming the upper-bound (lower-bound) radiative efficiency $\eta_R = 1$ ($\eta_R = 0.03$), we determine the T center bulk concentration $c_T = 8.2(2) \times 10^{10}$ cm^{-3} [$2.7(0.7) \times 10^{12}$ cm^{-3}]. T center formation in this sample is limited by the low residual carbon contamination of our sample (given in Appendix A).

Concentrations up to 200 times larger than this lower bound, at least 1.7×10^{13} cm^{-3}, have been produced in silicon photonics with use of a carbon implantation recipe [37]. Orders of magnitude increases in concentration have also been achieved with ion implantation for other radiation damage centers [49,50]. This bodes well for the feasibility of ^{28}Si ensembles with considerable optical depth. We expect at least an additional factor of 5 increase is possible over the (still sparse) T concentrations achieved by localized implantation reported in Ref. [37]. In the unit radiative efficiency case, this translates to a potential concentration increase factor of 1000. All other properties being equal, a 15-mm ^{28}Si crystal such as we measure with this T concentration will have optical depth $d = 27$, which is suitable for efficient quantum memory. We explore the optimal memory schemes for such an ensemble in Sec. VI.

It remains to be seen whether $c_T \sim 10^{14}$ cm^{-3} bulk ^{28}Si T ensembles can be achieved in practice. The localized implant recipes developed for integrated photonics do not translate directly to bulk crystals. New recipes should be developed for bulk ^{28}Si crystals grown with high carbon concentrations. It is not known what inhomogeneous broadening might be present in high-concentration ^{28}Si T center ensembles, and additional broadening will reduce the peak resonant OD (see Sec. VI for a discussion of inhomogeneous broadening in EIT and ATS memory schemes). However, implant-free T recipes in isotopically pure single-crystal silicon will likely achieve inhomogeneous linewidths far below those observed in SOI devices to date (limited by mass inhomogeneity and potentially device strain).

In addition to concentration or sample length increases, optical resonators can be used to increase the resonant OD of spin-photon ensembles. Many of the most efficient transduction demonstrations leverage optical resonators [23,24], although microwave-to-optical up-conversion has been demonstrated with 82% efficiency with a cavity-free atomic ensemble [22]. Silicon is a superb platform for monolithic resonators due to its extremely low intrinsic loss coefficient in the telecom bands (1.6×10^{-5} at 1326 nm [51]). Silicon Fabry-Perot and whispering gallery mode [52] resonators have been demonstrated with finesse many orders of magnitude beyond the $F \sim 1000$ required for efficient optical quantum memory with even the limited concentration of our ^{28}Si T sample. These resonators were manufactured from intrinsic float-zone silicon, but no performance reduction is expected with use of ^{28}Si. Even with the broader inhomogeneous linewidths that have been measured so far, the optical depth of high-density T centers implanted in natural silicon samples (9-GHz linewidth [45]) can be increased sufficiently for use as quantum memory with only the same $F \sim 1000$ low-finesse cavities.

Finally, ensembles can be incorporated into an integrated SOI photonic crystal [53] or waveguide ring cavities that deliver high optical confinement for an increased interaction strength. Typical intrinsic waveguide losses in such devices are approximately 2.5 dB/cm, imposing an upper limit on the effective ensemble length. High-OD integrated ensembles therefore require more than the factor of 5 concentration increase forecast above, or integrated inhomogeneous linewidths narrower than those demonstrated in natural silicon devices to date (18–50 GHz) [37,45], achieved, for example, by use of ^{28}Si SOI and less damaging alternatives to the T implant recipe. In Secs. VI–VIII we discuss the requirements for T center memories and microwave-to-optical transducers in terms of the OD and ensemble-resonator cooperativity. These platform-independent parameters apply equally to integrated and bulk crystal T ensembles.

In any case, it is necessary to consider how the inequivalent T center orientational subsets will impact memory performance. Memory schemes using only a single orientation will experience an optical depth penalty as high as a factor of 12, achieving a lower penalty depends on the orientation degeneracy for a chosen magnetic field direction. This orientation penalty would be reduced by the (untested) ability to form a given orientation preferentially.

IV. MICROWAVE COHERENT POPULATION TRAPPING

As a precursor to quantum memory protocols, we next demonstrate MW CPT [54] with another ^{28}Si T center ensemble. CPT is a quantum phenomenon in which an equilibrium atomic superposition is prepared by two coherent electromagnetic fields [55]. CPT underpins three-level coherent atom-light phenomena, including EIT [56] and stimulated Raman adiabatic passage. Observation of an EIT window requires sufficient ensemble absorption, but the accompanying CPT can be observed even in low optical depth ensembles by ODMR spectroscopy. The use of optical fields to generate coherent dark states has been extensively studied [57]. In comparison, relatively little effort has been focused on MW CPT [58–62].

The optical ground state of the T center under magnetic field B_0 has two possible microwave Λ schemes for coherently coupling the nuclear spin states $|1\rangle$ and $|2\rangle$ via the higher-energy electron spin states $|3\rangle$ and $|4\rangle$ as shown in Fig. 1. The T center is therefore a potential platform for Λ microwave quantum memory schemes.

To demonstrate this capability, a ^{28}Si T sample, prepared by the same method, is chosen for its narrow optical inhomogeneous linewidth $\Gamma^{\text{in}}/2\pi = 33$ MHz. A static magnetic field $B_0 = 80$ mT is applied along the [110] axis of the sample, splitting the TX_0 transition. Under this magnetic field, 10 of the 12 inequivalent orientational subsets i produce their own set of four optically resolved transitions A_i–D_i determined by the Landé g tensor of the anisotropic hole. Following Ref. [36], which used the same magnetic field configuration, we label the two remaining optically unresolved orientations $i = 1, 1'$. We may select distinct subsets for ODMR measurement by resonant optical excitation. For the following ODMR measurements, we choose the $i = 1, 1'$ subsets. Although these subsets are not optically resolved [36], we resolve the distinct orientations by CPT.

A "readout" laser resonant with C_1 selects these two optically degenerate subsets for ODMR spectroscopy. In the absence of any additional field, the readout simply pumps these two optically degenerate orientational subsets into the electron spin state $|\downarrow_e\rangle$, and this hyperpolarized ensemble does not fluoresce. Adding a single pump MW field that selects only one of the two hyperfine split states is still insufficient to prevent hyperpolarization, instead

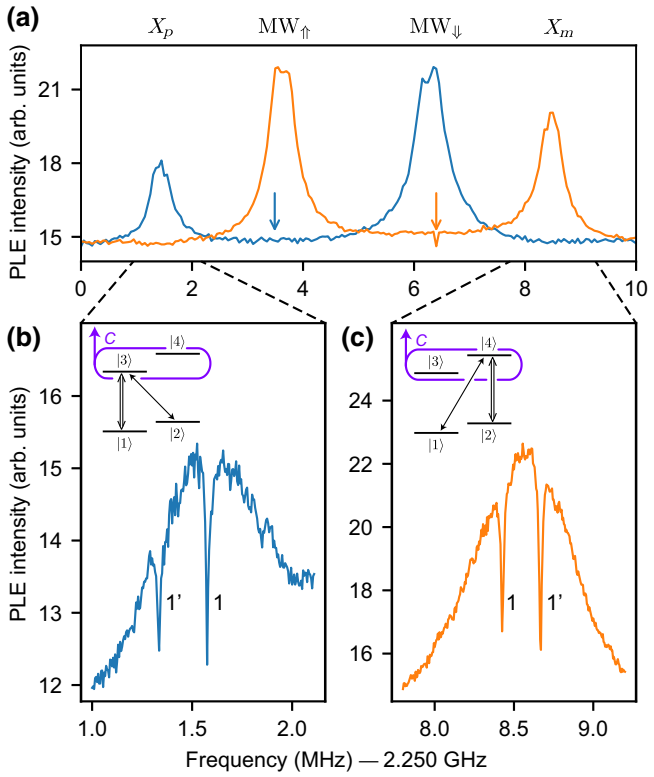

FIG. 3. ODMR spectra showing the sideband photoluminescence as a function of MW probe detuning. Resonant optical excitation of TX_0 C provides electron-spin-selective readout from $|\uparrow_e\rangle$. (a) Two of the four resonances $MW_{\Uparrow}$, $MW_{\Downarrow}$, X_p, and X_m are visible depending on the configuration of a MW pump (pump frequency arrow matches the corresponding spectrum color). The outer resonances are MW Λ configurations. (b),(c) High-resolution ODMR spectra of the Λ resonances showing narrow CPT dips at two-photon resonance for each of the 1 and 1′ orientation subensembles. The insets show energy level schemes showing the corresponding optical and MW configuration.

pumping the system to whichever of the hyperfine states $|1\rangle$ and $|2\rangle$ remains unaddressed. In these ODMR measurements, a MW "pump" is set resonantly with one of the four available MW transitions, and a MW "probe" scans all four transitions. Continuous photoluminescence is detected when the hyperfine states $|1\rangle$ and $|2\rangle$ are separately addressed by the MW fields. The ODMR spectra in Fig. 3(a) show two resonances per pump frequency. As expected, resonances involving the "forbidden" X_p and X_m are possible, but are weaker and narrower than resonances with only $MW_{\Downarrow}$ or $MW_{\Uparrow}$ [linewidths of 462(13), 506(9), 698(8), and 583(7) kHz, respectively].

CPT is evident in each of the two possible MW Λ configurations, shown in the inset in Fig. 3(a). When the MW fields are in two-photon resonance, CPT produces a dark state superposition of $|1\rangle$ and $|2\rangle$ that does not couple to the readout laser. Higher-resolution ODMR spectra in the

region of the two-photon resonances, Figs. 3(b) and 3(c), show CPT luminescence dips with a linewidth of 16(2) kHz—significantly narrower than the ODMR lines. For each configuration in Fig. 3 there are two dark resonances, one for each of the distinct orientational subsets 1 and 1′ and separated by 242(1) kHz, below the inhomogeneous linewidth and unresolvable by above-band PL or single-laser PLE. The low-power CPT linewidths are nuclear spin coherence limited, the coherence time is known to be longer than 1 s at 1.4 K [36]. However, at the microwave powers required to produce sufficient luminescence signal, these CPT linewidths are broadened by the microwave Rabi frequencies $\Omega_{\Uparrow}$, $\Omega_{\Downarrow}$, Ω_p, and Ω_m.

The observed ODMR and CPT profiles in Fig. 3 are the sum of fluorescence from the two near-degenerate orientational subensembles 1 and 1′, in proportion determined by the relative concentration and the dipole orientation. The precise ODMR peak associated with each ensemble is unknown. When one ensemble is in two-photon dark resonance, fluorescence from the remaining out-of-resonance ensemble is still present, with the effect that neither CPT dip apparently achieves complete fluorescence extinction as expected in the ideal low-power case.

Optically pumping transition C empties the states $|3\rangle$ and $|4\rangle$, rapidly destroying any coherence $\hat{\rho}_{34} = \langle 3|\hat{\rho}|4\rangle$, where $\hat{\rho}$ is the density matrix of the center, and power broadening the MW transitions. However, the choice to read using optical transition C is arbitrary, and we can invert the system to achieve two-photon coherence via the less common V scheme. Choosing transition B instead empties $|1\rangle$ and $|2\rangle$ and removes coherence $\hat{\rho}_{12}$. This configuration sustains nuclear spin coherences of the $|\uparrow_e\rangle$ hyperfine manifold, and we therefore expect CPT in V two-photon resonance, as shown in Fig. 4. The V CPT linewidths are 17(2) kHz, identical to the Λ case. The pump-probe MW frequency difference at each Λ or V CPT condition determines the effective hyperfine constants −2.93(1) MHz and −2.57(1) MHz for the 1 and 1′ subensembles, respectively.

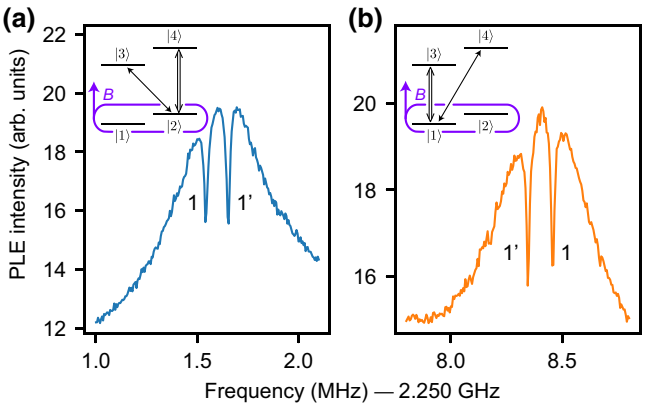

FIG. 4. ODMR spectra with optical readout via TX_0 B_1. In this configuration, CPT is possible in each of the two V schemes, insets in (a),(b) alongside the corresponding data. Coherences are prepared in the electron spin state opposite that in Fig. 3.

Dark CPT steady states decouple from the two fields in either the Λ configuration or the V configuration and cause a corresponding EIT window in the ensemble absorption. Absorption and dispersion manipulation by such EIT is the operational principle of EIT quantum memories. In Sec. VI we consider the prospects for T center EIT memories (both optical and microwave), but first we perform one final preparatory measurement. In the same Λ or V configuration, but in the limit of increasing pump power, the CPT window transitions to an Autler-Townes-split transition, which is itself the basis of an Autler-Townes quantum memory.

V. AUTLER-TOWNES SPLITTING

The operational bandwidth of EIT quantum memories is limited by the two-photon transition linewidth. AT quantum memories use selective absorption by the spectrally distinct AT-split dressed states of a single transition to circumvent this limit [12]. With a modified ODMR scheme, we can observe AT splitting of MW transitions in the same T ensemble. For this measurement, a slightly smaller magnetic field is chosen, $B_0 = 60$ mT along the [110] axis of the sample.

AT dressed states are split by the pump Rabi frequency Ω_p. Rabi frequencies fitted to the CPT notches above, and observed by EPR with the same apparatus [36], indicate that attainable AT splittings $\Omega_p = \Omega_{\Uparrow}$ or $\Omega_{\Downarrow} < 0.2$ MHz will not be clearly resolved with the ODMR schemes above. Instead, we apply an alternative ODMR scheme in which a rf probe field scans one of the NMR transitions. By this method we isolate a single subensemble and achieve ODMR linewidths narrow enough to measure the transition to AT splitting as Ω_p increases. Figure 5(a) shows ODMR spectra of the $|\uparrow_E\rangle$ nuclear transition rf probe field between states $|3\rangle$ and $|4\rangle$ as the MW power resonant with $MW_{\Uparrow}$ increases. We measure rf resonances AT-split by $\Omega_{\Uparrow}$, up to 55(1) kHz, demonstrating the basic mechanism required for microwave AT quantum memories. Splitting is limited in this case by the available MW power and the inefficient resonator design. Larger splittings for increased optical and MW memory bandwidths are possible. In the following section we compare EIT and AT memory models to assess the prospects of T center memories for microwave and optical fields, and determine the optimal bandwidth for operating T center memories at feasible optical depths.

VI. FREE-SPACE OPTICAL MEMORY

The coherence times of the T center electron and nuclear spins, $T_2^e > 2.1$ ms and $T_2^n > 1.1$ s, are appealing for quantum memory in either optical quantum networks or

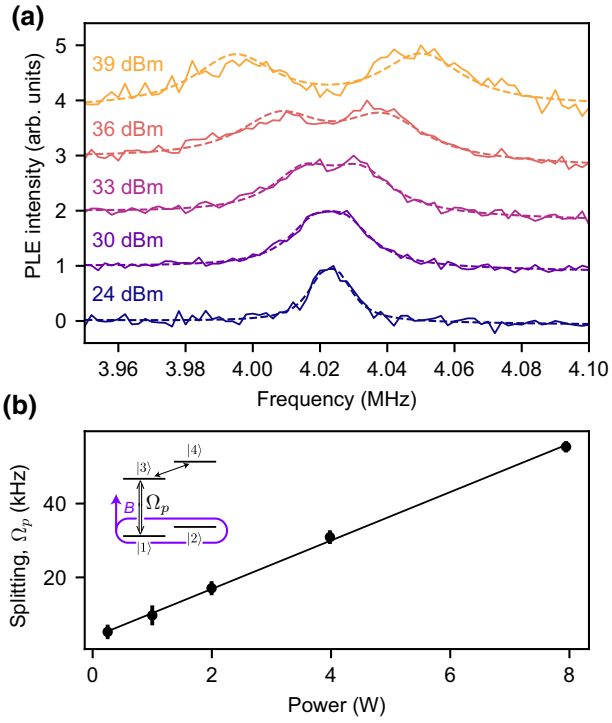

FIG. 5. Autler-Townes splitting of the $MW_{\Uparrow}$ transition as a function of $MW_{\Uparrow}$ power. (a) Spectra recorded by our scanning the nuclear flip transition with a non-phase-coherent rf source. The ODMR PL signal is generated by excitation to the TX_0 state by a laser resonant with the B_1 optical transition [scheme shown in the inset in (b)]. As the $MW_{\Uparrow}$ power (text labels) increases, AT splitting becomes clear. Dashed lines are a split-peak fit to each dataset. (b) Splitting from fits (equal to the $MW_{\Uparrow}$ Rabi frequency Ω_p) as a function of resonant power.

quantum processors. It remains to determine which of the many quantum memory schemes are best suited to the optical and microwave properties of T center ensembles determined in the literature and in the measurements reported above. Storage of a weak signal (i.e., probe) pulse using a relatively strong control field in a Λ-type system has been studied with different protocols, such as EIT, off-resonant Raman memories, and ATS [1,12,63,64]. Ensemble optical quantum memories have set milestones on multiple fronts. Optically deep atomic ensembles have achieved storage and recall efficiency of 92% by EIT [65]. Rare-earth ion crystal atomic frequency comb memories have demonstrated coherent storage for up to 1 h [10]. Gradient echo memory with atoms has achieved conditional storage fidelities of 98% at the single-photon level [66] and performance beyond the optical fiber limit [67]. Meeting these benchmarks on a single platform, let alone an integrated, telecom-band platform, remains a technical challenge.

If we ignore the nuclear spin, which is not optically resolved within inhomogeneous T centers measured to date, there are four optical transitions per center orientation that can be addressed individually and formed into two possible optical Λ configurations addressing the electron spin coherence. An optical-lifetime-limited T center optical quantum memory could directly address the longer-lived nuclear spin coherence, as in the MW memory proposal below, for storage times longer than 1 s. However, even the electron spin coherence time of approximately 2 ms is sufficient for a basic repeater demonstration, and swapping between the electron and nuclear spins is possible.

In this section we consider theoretically the Λ-type system comprising two long-lived ground states $|g_1\rangle = |\uparrow_e\rangle$ and $|g_2\rangle = |\downarrow_e\rangle$ that are optically connected to a common excited state $|\downarrow_h\rangle$. We assume both electron and nuclear spins are initially polarized. We then use a strong control field with the Rabi frequency Ω_c in resonance with the optical transition B ($\Omega_c = \Omega_B$) to store a weak signal pulse coupled to the A transition (see Fig. 1).

On the basis of the optical depth measurement reported in Sec. III, T center ensembles could be made with OD sufficient for resonant optical quantum memory schemes given feasible concentration increases. However, absent cavity-enhanced absorption, even these ODs are insufficient for off-resonance schemes, including gradient echo memory. Resonant memory schemes that efficiently use the available OD are best suited to near-term T center ensembles.

The narrowest T ensemble linewidth $\Gamma^{\text{in}}/2\pi$ measured to date is 33 MHz full width at half maximum (FWHM), where the total linewidth is a combination of inhomogeneous broadening, slow spectral diffusion, and the "instantaneous" homogeneous linewidth determined by dephasing (including spectral diffusion faster than the emission time) [36,45,46]. Optical memory schemes should consider each of these factors.

In EIT and ATS memory protocols, inhomogeneous broadening and spectral diffusion together decrease efficiency by reducing OD. We estimate potential resonant ODs from an ensemble with linewidth $\Gamma^{\text{in}}/2\pi =$ 56 MHz dominated by inhomogeneous broadening and potentially slow spectral diffusion. The slow spectral diffusion linewidth Γ^{SD} of T samples measured here was previously determined to be on the order of 27(12) MHz [45], and recent results indicate an instantaneous homogeneous linewidth $\Gamma^{\text{hom}}/2\pi$ of 0.69 MHz [46]. A dephasing-limited, or lifetime-limited, ensemble of the same concentration would have a correspondingly larger OD.

The effective OD for memory d' depends on the shape of the inhomogeneous profile and the retrieval direction. For example, in forward retrieval with Lorentzian broadening, $d' = d_0/(1 + \Delta_I/\gamma_e)$, where d_0 is the homogeneous OD, Δ_I is the half width at half maximum of the broadening profile, and γ_e is the polarization decoherence rate (the effective cooperativity of cavity-coupled memories

scales the same way) [68]. In this case, d' is the peak resonant OD, as reported in Sec. III. To deal with inhomogeneous broadening, one can consider spectral tailoring of the ensemble bounded from below by the homogeneous linewidth.

In the following subsections, we consider in detail the prospects of EIT and ATS free-space optical quantum memory schemes.

A. EIT memory

In the EIT protocol, a control field is used to store a signal field via a common optical excited state. The control field is chosen to be in two-photon resonance with the signal field and the ground states [8]. The control field induces a narrow transparency window in an otherwise opaque atomic system, and reduces the group velocity of the signal field. Once the signal is inside the atomic system, ramping down the control field power gradually to zero results in the adiabatic transfer of signal coherence to a collective spin excitation between the two ground state spin components (i.e., spin-wave mode). The signal remains spatially compressed inside the storage medium until reapplication of the control field.

EIT can be implemented effectively in both the narrowband regime, i.e., $B_{\mathrm{sig}} < \Gamma/2\pi$, and the broadband regime, i.e., $B_{\mathrm{sig}} > \Gamma/2\pi$, where B_{sig} is the bandwidth of the signal at full width at half maximum, and $\Gamma/2\pi$ is the homogeneous linewidth of the signal transition. However, this protocol is best suited for the narrowband regime, where control field optimization is achievable at any optical depth. Eliminating signal absorption and maintaining adiabatic evolution with a broad transparency window requires both a very large optical depth and a strong control field [69,70]. For these calculations, we pessimistically take the long-term spectral diffusion linewidth $\Gamma^{\mathrm{SD}} = 2\pi \times 27$ MHz as the relevant optical homogeneous linewidth Γ and $\gamma_e = \Gamma/2$ as the excited state decoherence rate. In practice, the memory timescale should be closer to the emission timescale, and $\Gamma = \Gamma^{\mathrm{hom}} = 2\pi \times 690$ kHz may be a fairer estimate.

In general, EIT efficiency may be optimized through control field and/or signal pulse shaping [71–73]. The consistency of these optimization methods was demonstrated in Ref. [74]. In the narrowband regime and for $d' > 20$, control field optimization is achievable by keeping the process adiabatic while satisfying the condition $\tau_d/\tau_{\mathrm{sig}} \sim 2$, where $\tau_d = \Gamma/\Omega_c^2$ is the group delay and τ_{sig} is the signal time at the FWHM [70]. Considering a probe field with a Gaussian temporal profile, the control optical Rabi frequency Ω_c should therefore satisfy the condition $\Omega_c^2 \sim d\Gamma B_{\mathrm{sig}}/0.88$.

For T center ensembles with an effective optical depth d' of, for example, 10, 20, 30, or 40, the maximum achievable efficiency of the EIT protocol for the forward retrieval can be estimated as approximately 53%, 65.7%, 73%, and 77%, respectively [71,74]. The back-retrieval memory efficiency depends on the ground state splitting $\omega_{g_1g_2}$ (as nonzero splitting breaks the conservation of momentum in backward retrieval [71]). Therefore, for a nonzero splitting, the backward efficiency could be lower than the efficiency of forward retrieval unless we make $\sqrt{d'} \gg L\omega_{g_1g_2}/c$, where L is the length of the medium and c is the speed of light.

These EIT efficiency estimates apply for short storage times. Spin decoherence can be taken into account by adding the term $\exp(-t/T_2)$ to the efficiency during the storage time [71,74]. Other imperfections, such as four-wave mixing (FWM) [74,75], may further reduce experimentally achievable efficiencies.

B. ATS memory

Unlike the EIT protocol, which relies on adiabatically eliminating the atomic polarization mode, in ATS memory, polarization mediates the nonadiabatic coherence exchange between signal pulse and spin modes. In the broadband regime, ATS memory is less demanding in terms of technical requirements, such as optical depth and control field power, compared with EIT memory. However, in the narrowband regime, the efficiency of ATS memory is close to zero as the average coherence time of the transitions in resonance with the signal and control fields becomes shorter than the interaction time (i.e., signal pulse duration).

Assuming the system is initially prepared in the state $|g_1\rangle$, we can use dynamically controlled ATS lines produced by a strong control field that drives the $|g_2\rangle$-$|e\rangle$ transition to absorb a weak signal pulse in resonance with the $|g_1\rangle$-$|e\rangle$ transition [12]. Absorption of the signal pulse by ATS peaks (with a peak separation equal to the control Rabi frequency) will then map its coherence to a collective state between $|g_1\rangle$ and $|e\rangle$ (i.e., polarization mode), which subsequently evolves into a collective spin excitation between the ground states. After the write (i.e., storage) process, we abruptly switch the control field off to trap the coherence, wait for the storage time, and turn control field on again for the readout (i.e., retrieval) process. Using control field optimization, one can increase the spectral overlap between the ATS peak separation and the signal bandwidth to maximize signal pulse absorption. Here, the control field optimization requires the control pulse area for both the write stage and the read stage to be 2π [70]. Using the ATS memory protocol for the T center, one can achieve a relatively high efficiency for broadband light storage and retrieval.

In Ref. [12], ATS memory efficiency in free space is discussed in terms of the ATS factor $F = \Omega_p/\Gamma$ (or equivalently $F = 2\pi B_{\mathrm{sig}}/\Gamma$). Figure 6 shows ATS memory efficiency as a function of effective optical depth. Here

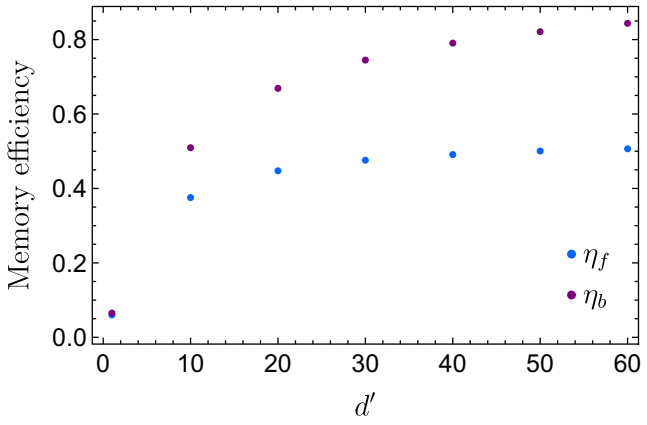

FIG. 6. Maximum free-space ATS memory efficiency for forward (η_f) and backward (η_b) retrieval with respect to the effective optical depth in the broadband regime.

the efficiencies are maximized with respect to the factor F. As an example, for $d' = 20$, the maximum efficiency $\eta_{b,\max} = 67\%$ ($\eta_{f,\max} = 44.7\%$) for $F = 3.28$ ($F = 5.5$) is achievable in the backward (forward) propagation. These F values correspond to Rabi frequencies Ω_p of $2\pi \times 88.6$ MHz and $2\pi \times 148$ MHz for the backward and forward modes, respectively, with $\Gamma = \Gamma^{\mathrm{SD}}$. With the instantaneous linewidth $\Gamma = \Gamma^{\mathrm{hom}}$, the required powers are a factor of 40 lower. To avoid excess heating in the system due to the control field, one can reduce the spot size (i.e., use a focused beam). The necessary spot size is set by the cooling power of the cryostat, thermal coupling, and the percentage of absorbed power.

VII. MICROWAVE MEMORY

We now turn our attention to T center prospects for MW quantum memories. In Secs. IV and V we reported coherent MW interactions in T center ensembles from the CPT regime to the AT regime. MW AT splitting such as we observe is a precursor to the demonstration of an ATS MW memory. We treat such an ATS memory theoretically to determine the prospects of MW memories with near-term T center ensembles. For this study of the MW ATS memory, we choose one of the two possible MW Λ schemes shown in Sec. IV, assigning $|1\rangle$ and $|2\rangle$ as ground states $|g_1\rangle$ and $|g_2\rangle$, respectively, and $|3\rangle$ as excited state $|e\rangle$. We begin with an initial state $|g_1\rangle$, and use dynamically controlled ATS lines produced by a control field, as observed in Sec. V, to store a signal field resonant with the $\mathrm{MW}_{\Uparrow}$ transition (see Fig. 1) so that the coherence of the signal pulse is mapped into the collective nuclear spin excitations of the atoms. The theoretical treatment from Ref. [12] applies to the ATS MW memory as well as the optical memory considered above. The T level used as an excited state in this MW memory scheme is much longer lived and more coherent than the TX_0 level used in the optical memory scheme. The decoherence rate $\gamma_e = 1/T_2^e = 2\pi \times 76$ Hz, and even the broadened, inhomogeneous ODMR linewidths reported in Sec. IV are narrower than for the optical transitions.

The MW ATS memory requires correspondingly lower Ω_p; however, in general, the weakness of magnetic dipole transitions requires a MW resonator to increase the MW-ensemble coupling strength g. Specific MW resonator geometries are considered, for example, in Ref. [27]. To describe this resonantly enhanced interaction, we can use the cavity input-output formalism i.e., $\hat{E}_{\mathrm{out}} = -\hat{E}_{\mathrm{in}} + \sqrt{2\kappa}\hat{E}$, and the Heisenberg equations of motion [12,76]:

$$\begin{aligned}\dot{\hat{P}} &= -\gamma_e \hat{P} + ig(t)\sqrt{N}\hat{E} + \frac{i}{2}\Omega_p \hat{S},\\ \dot{\hat{S}} &= \frac{i}{2}\Omega_p^* \hat{P},\\ \dot{\hat{E}} &= ig(t)\sqrt{N}\hat{P} - \kappa\hat{E} + \sqrt{2\kappa}\hat{E}_{\mathrm{in}},\end{aligned} \tag{2}$$

where $\hat{P}$ and $\hat{S}$ are the polarization and spin-wave operators, $\hat{E}$ is the cavity field, which we assume can be adiabatically eliminated, $2 \times \kappa$ is the cavity decay rate, $\gamma_e = \Gamma/2$ is the decoherence rate of $|3\rangle$, $g(t)$ is the time-dependent light-matter coupling per emitter, and N is the number of atoms in the ensemble. Note that here we have ignored the Langevin noise operators (i.e., the incoming noise is vacuum noise) and once again have assumed the spin-wave decoherence rate is negligible as per Sec. VI.

To estimate the overall efficiency of the memory in the presence of a resonator, we follow the same optimal scheme as in Ref. [76] for the nonadiabatic or fast limit $\Omega > \Gamma C$, where C is the cooperativity parameter, $C = Ng^2/\kappa\gamma_e$. The overall efficiency $\eta = \eta_s\eta_r$, is the product of the optimal storage efficiency η_s (average ratio of stored excitations to incoming photons) and the optimal retrieval efficiency η_r (average ratio of re-emitted photons to stored excitations). In the optimal regime, we compute the retrieval efficiency as

$$\eta_r = \int_0^{t_r} dt \frac{2N}{\kappa} g^2(t) e^{-\int_0^t dt' 2(Ng^2(t')/\kappa + \gamma_e)}, \tag{3}$$

where t_r is the effective time elapsed during the retrieval process. For simplicity, it is assumed that the retrieval process starts at $t = 0$ rather than at some time $t_s > \tau$, where τ is the duration of the signal, and that $S(0) = 1$ and $P(0) = 0$. It has been shown that with the optimal strategy, the storage and retrieval efficiencies are analogous [76–78]. Hence, in the optimal regime, the overall efficiency can be estimated as follows:

$$\eta \sim \frac{C'^2}{(1+C')^2}\left(1 - e^{-2\gamma_e(1+C')t_s}\right)\left(1 - e^{-2\gamma_e(1+C')t_r}\right), \tag{4}$$

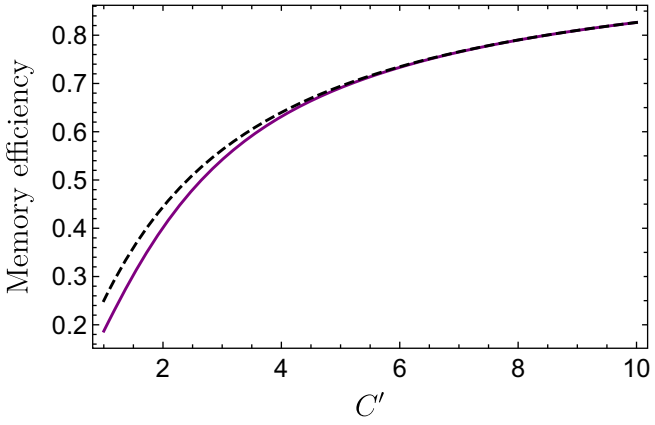

FIG. 7. Memory efficiency as a function of the resonator effective cooperativity. The solid line shows the efficiency given by Eq. (4) assuming $t_s = t_r = 1/2\gamma_e$. The dashed line corresponds to $t_r \to \infty$ [i.e., $\eta = C'^2/(1+C')^2$].

where C' is the reduced cooperativity (i.e., effective cooperativity) in the presence of the inhomogeneous broadening. In the derivation of Eq. (4), it is assumed that during the retrieval process all spin mode excitations have been evolved back to the polarization mode (i.e., no excitations are left in the spin mode). For fixed and finite values of the effective times, as the cavity cooperativity increases, the exponentially decaying terms in Eq. (4) go to zero, and hence the first term dominates. Equivalently, in Eq. (3), if we initially assume $t_r \to \infty$ such that no excitations are left in the T ensemble, i.e., $P(\infty) = 0$, the optimal retrieval efficiency reduces to $C'/(1+C')$ and the overall efficiency becomes $C'^2/(1+C')^2$ (see Fig. 7) [76]. With this maximum possible efficiency, one can store photons with $\tau \sim 1/C'\gamma_e$, where the polarization decay rate is negligible.

From this analysis we can see that resonator cooperativities of order 10 are required to exceed 80% memory efficiency with a T center ensemble. Although we introduced them in the context of the MW memory scheme, the expressions in Eq. (2) apply to resonantly enhanced optical memories as well. In the following section we propose combining resonantly enhanced MW and optical memories to realize a T center MW-to-optical transducer with T center ensembles.

VIII. MICROWAVE-TO-OPTICAL TRANSDUCTION

Motivated by the optical and microwave memory performance estimates above, we now look at combining the capabilities to form a T center ensemble microwave-to-optical transducer that stores MW photons as spin-wave excitations and recalls them optically. For this operation we consider both resonantly enhanced optical and microwave ATS memories.

Transduction may be achieved by way of two Λ schemes, optical and microwave, addressing the same spin coherence. If this cannot be achieved, it is necessary to transfer the coherence by an intermediate step. In the following, we elaborate on three possible approaches.

First, we may consider the MW and optical Λ schemes set out in Secs. VI and VII. The MW configuration uses the long-lived nuclear spin coherence ρ_{12}; however, as discussed in Sec. VI, the hyperfine splitting between $|1\rangle$ and $|2\rangle$ may not be optically resolved. Transduction from this microwave interface to an optical field using the same optical Λ scheme we used in Sec. VI for an optical AT memory requires one to (1) store MW photons in resonance with the $|1\rangle$-$|3\rangle$ transition as nuclear spin-wave excitations between states $|1\rangle$ and $|2\rangle$, (2) transfer the nuclear spin wave ρ_{12} to an electron spin wave ρ_{13}, and (3) recall the stored pulse using a control field in resonance with the optical transition B_1. Transferring coherence between the nuclear and electron spin waves (step 2) requires only coherent control of the T center ground states, which has already been demonstrated [36].

Alternatively, one may consider schemes that avoid step 2 above. One option is to use the electron spin for MW storage via a different Λ configuration i.e., $|1\rangle$ and $|3\rangle$ as the ground states, and $|4\rangle$ as the excited state. This configuration allows us to store MW photons in resonance with the $|1\rangle$-$|4\rangle$ transition while the control field is resonant with the $|3\rangle$-$|4\rangle$ transition. Note that the decoherence rates of the $|1\rangle$-$|3\rangle$ and $|1\rangle$-$|4\rangle$ transitions are comparable. In general, this results in ATS line broadening and reduced efficiency [12]. However, in the limit where the electron spin coherence time is very long, as it is in the T center [36], such ATS line broadening is negligible.

Finally, the transfer step is unnecessary when the hyperfine splitting of the nuclear spin wave is optically resolved; for example, in a scheme that uses larger hyperfine splittings due to nuclear spins at the carbon sites in ^{13}C isotopic variants of T [36], at higher magnetic fields, or by increasing the optical linewidth such that the hydrogen hyperfine splitting is resolved. This way one can consider $|1\rangle$ and $|2\rangle$ as the joint ground states, and $|3\rangle$ and $|\downarrow_h\rangle$ as the excited state of the MW and optical Λ systems, respectively. However, we see that four-wave-mixing noise is prohibitively high in this configuration.

A. Transduction efficiency and fidelity

Optimal efficiency of the transducer, where MW and optical transitions are coupled to the respective cavities, can be estimated with use of the same optimal strategy as for the ATS memory except that there is now an additional mode mismatch factor η_m that should be taken into account. As a result, the overall efficiency will be expressed as $\eta = \eta_s\eta_r\eta_m$. The mode mismatch factor depends on the design (geometry) of the cavities. In the

ideal case, where all atoms are placed in the maximum of both the optical field and the MW field, the mode mismatch factor can reach unity. In this case and for $t_r \to \infty$, the optimal efficiency of the transducer is estimated as $C_s' C_r'/(1 + C_s')(1 + C_r')$, where C_s' and C_r' are the effective cooperativity of the MW and optical cavities, respectively.

The other metric to quantify the quality of transduction is the overlap between the transduced signal and the transduced noise. We refer to this measure as the "transduction fidelity." To compute the fidelity, one could solve the system dynamics by taking several important imperfections, such as spin decoherence, microwave thermal photons, optical noise photons, and inhomogeneous broadening, into account. Spin decoherence is negligible given that the process can be much faster than the spin coherence times [36]. Inhomogeneous broadening can be dealt with by spectral tailoring. Therefore, here we consider only the thermal microwave and optical photon noise sources. For this calculation, we consider a transduction system consisting of $|1\rangle$ and $|3\rangle$ as the ground states, and $|4\rangle$ and $|\downarrow_h\rangle$ as the excited state of the microwave and optical Λ subsystems, respectively.

Typically for optically pumped transduction and memory schemes, the optical pump itself is a source of optical noise that must be removed [67,79,80]. In Sec. VI, we estimated Ω_p as high as $2\pi \times 148$ MHz. This translates to optical pump intensities $I_{\text{pump}} \sim 30$ mW/mm^2. We note that this estimate is from the long-term spectral diffusion linewidth Γ^{SD}, and the power is correspondingly lower for smaller linewidths. In this cavity-enhanced transduction scheme, the output I_{pump} will be lower, but it remains necessary to separate the pump from the signal by a combination of spatial and spectral filtering. Although considerable effort is required, this is a common challenge for such schemes and depends sensitively on specifics of the platform and cavity design that are outside of the scope of this work. There are, however, sources of optical noise in the signal mode that need to be considered.

FWM is an intrinsic source of optical noise photons in this scheme. For this set of energy levels, the infidelity induced by FWM depends critically on the total decoherence rate of $|\downarrow_h\rangle$ during the (optical) recall step, γ_e^r. This can be seen by computing the FWM strength parameter $x = C'\gamma_e^r/\omega_{13}$, where C' is the effective cooperativity for the optical cavity. When $x \ll 1$, the fidelity is well approximated as $F_{\text{FWM}} \sim \exp(-\sqrt{3}C' 4\pi^2 x^2)$ for single-photon signals [75]. To quantify the FWM infidelity, we take the electron spin splitting, $\omega_{13} = 2\pi \times 2.25$ GHz, from the measurements reported in Sec. IV. The relevant decoherence rate depends on the FWM and spectral diffusion timescales. The total decoherence implied by long-term homogeneous linewidth measurements is given by $\gamma_e^r = 2\pi \times 27/2$ MHz [45], which leads to $x = 0.06$ and very low fidelity, $F_{\text{FWM}} = 0.085$. On the other hand, the total decoherence rate relevant over the emission timescale is much lower, $\gamma_e^r = 2\pi \times 0.690/2$ MHz [46], and gives negligible FWM infidelity, $x \sim 1.5 \times 10^{-3}$ and $F_{\text{FWM}} \sim 0.998$. For this material the true FWM strength lies somewhere between these two bounds. Given that the FWM process timescale is not considerably longer than the excited state lifetime, the lower bound is the fairer estimate, and it seems likely that FWM infidelity can be made negligible at this magnetic field. In an alternative configuration reading from the nuclear spin ground states $|1\rangle$ and $|2\rangle$, FWM noise is prohibitive even at the optical-lifetime linewidth limit.

Reducing the thermal MW noise requires significantly lower temperatures than required by the T center alone. The initial microwave thermal occupation $n_{\text{th}} = 1/(e^{(\hbar\omega_{1,4}/k_B T)} - 1)$ is estimated to be 0.0045 with $T = 20$ mK and $\omega_{1,4} = 2\pi \times 2.255$ GHz [36], which is the splitting between $|1\rangle$ and $|4\rangle$. Since the initial microwave photon occupation is quite small, and it does not affect the quantum system dynamics significantly, we can treat it as a perturbation. The fidelity accounting for thermal population can be computed with use of the signal-to-noise ratio (SNR) [27]:

$$F_{\text{TP}} = \frac{1}{1 + \text{SNR}^{-1}}. \tag{5}$$

Given that the thermal noise is treated as a perturbation, it is valid to compute the SNR before the transduction process starts. In this way, the SNR is given by

$$\text{SNR} = \frac{n_{\text{sig}}}{n_{\text{th}}}, \tag{6}$$

where n_{sig} is the mean occupation of the signal in the microwave cavity. For a single-photon signal, $n_{\text{sig}} = B_{\text{sig}}/2\kappa_s$, where $2 \times \kappa_s$ is the microwave cavity decay rate. This is valid in the regime where $B_{\text{sig}} \ll \kappa_s$. Given that $n_{\text{th}} \ll n_{\text{sig}}$, the fidelity shown in Eq. (5) can be simplified as

$$F_{\text{TP}} \sim 1 - \frac{n_{\text{th}}}{n_{\text{sig}}} = 1 - \frac{2n_{\text{th}}\kappa_s}{B_{\text{sig}}}. \tag{7}$$

Since we are interested in the case where the transduction efficiency is maximized, B_{sig} can be expressed as $B_{\text{sig}} = C_s'\gamma_e^s$, where γ_e^s is the decoherence rate of the polarization mode we use during the "storage" process. Hence, in the regime of maximum efficiency, the fidelity is explicitly given by

$$F_{\text{TP}} \sim 1 - \frac{2n_{\text{th}}\kappa_s}{C_s'\gamma_e^s}. \tag{8}$$

Clearly, as the cavity cooperativity increases, the fidelity increases, and the efficiency also increases, as shown in Fig. 7.

The other way to compute the fidelity is to estimate the SNR after the transduction, which should be equivalent to the approach discussed above. In this way, we can model the microwave thermal photons as dark counts [81]. The dark count rate is given by $D = R\eta$, with the transduction efficiency η and the average rate of production of thermal photons R. It describes the effective number of photons emitted as background noise in the optical cavity per unit of time. The probability distribution associated with this dark count rate is given by a Poisson distribution: $P(T_{\mathrm{tr}}, D) = D^n T_{\mathrm{tr}}^n e^{-DT_{\mathrm{tr}}}/n!$, where n is the number of dark counts and T_{tr} is the total transduction time. Thus, this time can also be written as $T_{\mathrm{tr}} = t_s + t_r$.

Then, for a single-photon transduction, the SNR takes the following form:

$$\mathrm{SNR} = \frac{\eta n_{\mathrm{sig}}}{\overline{N}_D}, \tag{9}$$

where $\overline{N}_D$ is the mean number of dark counts. Specifically, at a given time T_{tr}, the SNR can be expressed as

$$\mathrm{SNR} = \frac{\eta n_{\mathrm{sig}}}{DT_{\mathrm{tr}}}, \tag{10}$$

where DT_{tr} is the mean number of dark counts that follow the Poisson distribution. It can be further simplified as $\mathrm{SNR} = n_{\mathrm{sig}}/RT_{\mathrm{tr}}$. In the regime of maximum efficiency, $RT_{\mathrm{tr}} = n_{\mathrm{th}}$, we recover $\mathrm{SNR} = n_{\mathrm{sig}}/n_{\mathrm{th}}$, which leads to the fidelity shown in Eq. (8).

IX. DISCUSSION

The T center appears to combine several properties appealing for both microwave and quantum memories, and transduction between them, including long-lived spins and telecom optical emission. We have considered possible quantum memory and transduction schemes for ensembles of T centers, and performed preliminary measurements with ensembles in ^{28}Si to establish properties informing memory and transduction device design.

Absorption measurements indicate a resonant optical depth of 0.009 in a narrow-linewidth ensemble. Cautiously forecasting a small increase over T center concentrations that have already been demonstrated in devices, we project that an optical depth of 27 with a similar sample is possible. This optical depth is sufficient for efficient optical quantum memory by EIT or ATS with an estimated memory efficiency as high as 73%.

For a repeater scheme based on a deterministic single-photon source and single-photon Bell state measurement [82], repeater rates of 10 Hz (1 Hz) are achievable over 100 km with memory efficiency of 80% and memory lifetime of 30 ms (1.2 ms) (see Fig. 5 in Ref. [83] for more information). Reducing the memory efficiency to 60% results in a repeater rate of 1 Hz with a memory lifetime of 6.5 ms. With use of a deterministic photon-pair source and two-photon Bell state measurement scheme [84], a memory efficiency of 60% (80%) with a lifetime of 1.1 ms (0.5 ms) results in a repeater rate of 1 Hz over 100 km [83].

In addition to the potential for optical memory, the T center's optical ground state spin structure features Λ and V configurations suitable for storing MW fields. We demonstrated these configurations by ODMR spectroscopy, and measured CPT windows in Λ and V configurations as a precursor to an EIT memory for MW fields. Fluorescence SNR requirements prohibit us from reaching the low-power limit, but even so we measured CPT linewidths of 17(2) kHz, significantly below the ODMR linewidth, and resolved orientation subensembles that were degenerate to MW ODMR precision. We demonstrated microwave ATS up to 55(1)-kHz splitting. We then discussed a cavity-enhanced MW memory protocol and arrived at an efficiency estimate as a function of cavity cooperativity. In particular, MW memory efficiencies greater than 80% are possible for $C' = 10$.

In general, the operation of MW and optical T center quantum memories can be combined for transduction between the microwave and optical fields. Transduction requires (1) an optical quantum memory addressing the nuclear spin coherence ρ_{12}, (2) a microwave memory addressing an electron spin coherence such as ρ_{13} via an NMR control field, or (3) coherent transfer between ρ_{12} and ρ_{13} at an intermediate stage. Condition 3 requires only the coherent control of T ensembles, which has already been experimentally demonstrated [36]. Furthermore, condition 1 is within reach of schemes using the known ^{13}C T center variants.

We proposed a transduction protocol where both microwave and optical transitions are coupled to resonators, and discussed the efficiency and fidelity of the system. Mutually compatible MW and optical cavities with $C' = 10$ would yield microwave-to-optical transduction efficiencies of 83%. Necessary future work includes further increasing ensemble concentrations, and engineering optical and microwave resonators meeting the requisite cooperativities and mode overlap, but an in-principle T center transduction demonstration could be achieved with designs available in the literature.

Compared with electro-optomechanical and electro-optical transduction, which need mechanical motion and electro-optical active materials, respectively, to mediate the coupling between optical and microwave systems, atomic-based transducers benefit from having both optical and microwave addressable transitions. Hence, to date, several transduction schemes based on atomic ensembles have been proposed. For example, Williamson *et al.* [26], predicted that using off-resonant fields and satisfying an impedance-matching condition between optical and microwave cavities would result in conversion efficiency close to unity. However, fulfilling this condition requires

the product of the cavities' cooperativities to be made large, which may not be obtainable or favorable in some systems. Recently, microwave-to-optical transduction in Rydberg atoms using six-wave mixing and off-resonant scattering techniques was demonstrated [22]. Although an impressive efficiency of 82% was achieved in that experiment, it remains very difficult to cool and trap atoms near superconducting waveguides, and that system is not compatible with telecom wavelengths.

Some of us recently proposed a transduction scheme using rare-earth-ion-doped (^{167}Er-doped) crystals at zero external field [27]. This scheme also requires two cavities coupled to the optical and microwave transitions and emits telecom-band optical photons. However, a much higher cooperativity ($C' \gg 10$) is required to achieve an efficiency of 86% in this transducer. Furthermore, the T center's energy level structure is much simpler than that of ^{167}Er (which has nuclear spin $I = 7/2$), allowing simpler control and transduction schemes.

We have demonstrated the potential of this spin-photon platform for quantum memory, and identified pathways toward efficient microwave-to-optical transduction with T centers. Further developing and transplanting this approach into on-chip devices (for example, with integrated silicon photonic resonators combining moderate mode confinement and high-quality factors) would yield an on-chip spin-photon interface for quantum memories and microwave-to-optical transducers. These devices could network directly between quantum information platforms that share the same technologically and commercially advanced silicon chip platform (including superconducting qubits, quantum dots, trapped ions, and silicon impurity spins) and the telecom optical fibers of a global quantum internet.

ACKNOWLEDGMENTS

This work was supported by the Natural Sciences and Engineering Research Council of Canada, the New Frontiers in Research Fund, the National Research Council of Canada through its High-Throughput Secure Networks challenge program, the Canada Research Chairs program, the Canada Foundation for Innovation, the B.C. Knowledge Development Fund, and the Canadian Institute for Advanced Research Quantum Information Science program. D.B.H. is supported by the Banting Fellowship program.

The ^{28}Si samples used in this study were prepared from the Avo28 crystal produced by the International Avogadro Coordination (2004–2011) in cooperation among the International Bureau of Weights and Measures, the Italian National Institute of Metrology Research, the Institute for Reference Materials and Measurements (European Union), the Australian National Measurement Institute, the National Metrology Institute of Japan, the National Physical Laboratory of the United Kingdom, and the Physikalisch-Technische Bundesanstalt (Germany). We thank Alex English of Iotron Industries for assistance with electron irradiation.

APPENDIX A: SAMPLE PREPARATION

All measurements are performed on one of two ^{28}Si crystals, previously described in Ref. [36]. These were purified to 99.995% ^{28}Si isotope proportion by the International Avogadro Coordination and then electron irradiated and thermally annealed to produce T. In addition to isotopic purity, these samples have low chemical impurity, with less than 10^{14} O_2/cm^3. T centers are formed from naturally present low-level carbon impurities, which differ between the two samples. The sample used for absorption measurements has 1.5×10^{15} C/cm^3, and the sample used for CPT and ATS measurements has 5×10^{14} C/cm^3.

APPENDIX B: METHODS

1. Cryogenics

The samples are loosely mounted in a liquid-helium immersion Dewar vessel such that the crystal is not strained. The temperature of the ^{4}He bath is adjusted between 1.4 and 4.2 K by pressure control.

2. Photoluminescence spectra

The sample is illuminated with an above-band-gap 1047-nm laser, and the resulting broadband photoluminescence is directed into a Bruker IFS 125 HR FTIR spectrometer with a CaF_2 beam splitter and a liquid-nitrogen-cooled Ge photodetector.

3. Absorption measurement

The sample is illuminated along its longest side by a broadband light source with beam size smaller than the sample cross section. Light passes through the sample and two cryostat windows before being directed into the Bruker FTIR spectrometer. The light source spectrum is free of structure in the vicinity of the T center absorption lines and is removed by subtraction of a linear fit about the absorption dip location.

4. Photoluminescence excitation

Photoluminescence excitation spectra are recorded by our scanning the TX_0 ZPL with a narrow, tunable laser and detecting lower-energy photons emitted into the TX phonon sideband. Resonant excitation is performed with a Toptica DL100 tunable diode laser. The optical power is amplified up to 100 mW with a Thorlabs BOA1017P amplifier, and the beam is expanded to a diameter of 2–4 mm. Nonresonant excitation light due to spontaneous emission in the laser and amplifier is removed by

a combination of an Edmund Optics 87-830 1350 ± 12.5 nm band-pass filter and an Iridian Spectral Technologies DWDM 1329 ± 0.5 nm band-pass filter. The two filters are tilted so as to tune them onto the TX_0 resonance.

Stray excitation light is removed from the detection path by two Semrock BLP02-1319R-25 1319-nm long-pass rejection filters, which block the excitation light at TX_0 with an optical density of 4.5 at normal incidence, but pass light with wavelength longer than 1350 nm. A 1375(50)-nm band-pass filter further selects a detection window in the TX phonon sideband that excludes a silicon Raman replica of the pump laser at 1426 nm. The fluorescence rate in this detection window is measured by an IDQuantique ID230 avalanche photodiode with 25% quantum efficiency.

5. Optically detected magnetic resonance

Magnetic resonance experiments are performed with the sample in an adjustable magnetic field applied by an iron core electromagnet within the PLE apparatus as described above. The sample is held at the center of a split-ring resonator with a resonant frequency of 2.25 GHz and a bandwidth of 10 MHz. MW signals from two signal generators (Stanford Research Systems SG384 and SG386) are combined with a ZB2PD-63-S+ power splitter (Minicircuits) and then amplified up to a power of 1 W by ZHL-16W-43-S+ (Minicircuits) and ZHL-1-2W+ amplifiers (Minicircuits) as required.

APPENDIX C: NOTATION KEY

t_r: Duration of the recall (optical) transduction step.

t_s: Duration of the storage (MW) transduction step.

X_r or X^r (where X is any variable): X specifically for the recall stage of the transduction protocol.

X_s or X^s (where X is any variable): X specifically for the storage stage of the transduction protocol.

Γ: Homogeneous FWHM linewidth of the excited state ($|{\downarrow}\,\mathrm{H}\rangle$ for optical Λ schemes, and $|3\rangle$ for MW Λ schemes).

γ_e: Excited state decoherence rate ($|{\downarrow}\,\mathrm{H}\rangle$ for optical Λ schemes, and $|3\rangle$ for MW Λ schemes).

Γ^{hom}: Measured "instantaneous" homogeneous linewidth [includes contributions from fast (less than 1 μs) spectral diffusion, dephasing, and lifetime].

Γ^{in}: Measured inhomogeneous FWHM linewidth (includes contributions from static inhomogeneous broadening, spectral diffusion, dephasing, and lifetime).

Γ^{SD}: Measured long-term homogeneous (spectral diffusion) FWHM linewidth (includes contributions from slow and fast spectral diffusion, dephasing, and lifetime).

Ω_c: EIT control field Rabi frequency ($\Omega_c = \Omega_B$ for the optical EIT scheme considered).

Ω_p: Control field or ATS pump Rabi frequency ($\Omega_p = \Omega_B$ for the optical ATS scheme considered, and Ω_{X_p} for the MW ATS scheme)

[1] A. I. Lvovsky, B. C. Sanders, and W. Tittel, Optical quantum memory, Nat. Photonics **3**, 706 (2009).

[2] H.-J. Briegel, W. Dür, J. I. Cirac, and P. Zoller, Quantum Repeaters: The Role of Imperfect Local Operations in Quantum Communication, Phys. Rev. Lett. **81**, 5932 (1998).

[3] L. Childress, J. Taylor, A. S. Sørensen, and M. D. Lukin, Fault-tolerant quantum repeaters with minimal physical resources and implementations based on single-photon emitters, Phys. Rev. A **72**, 052330 (2005).

[4] N. Sangouard, C. Simon, H. De Riedmatten, and N. Gisin, Quantum repeaters based on atomic ensembles and linear optics, Rev. Mod. Phys. **83**, 33 (2011).

[5] F. K. Asadi, N. Lauk, S. Wein, N. Sinclair, C. O'Brien, and C. Simon, Quantum repeaters with individual rare-earth ions at telecommunication wavelengths, Quantum **2**, 93 (2018).

[6] H. J. Kimble, The quantum internet, Nature **453**, 1023 (2008).

[7] E. Gouzien and N. Sangouard, Factoring 2048-Bit RSA Integers in 177 Days with 13 436 Qubits and a Multimode Memory, Phys. Rev. Lett. **127**, 140503 (2021).

[8] M. Fleischhauer, A. Imamoglu, and J. P. Marangos, Electromagnetically induced transparency: Optics in coherent media, Rev. Mod. Phys. **77**, 633 (2005).

[9] M. Afzelius, C. Simon, H. De Riedmatten, and N. Gisin, Multimode quantum memory based on atomic frequency combs, Phys. Rev. A **79**, 052329 (2009).

[10] Y. Ma, Y. Z. Ma, Z. Q. Zhou, C. F. Li, and G. C. Guo, One-hour coherent optical storage in an atomic frequency comb memory, Nat. Commun. **12**, 1 (2021).

[11] B. Kraus, W. Tittel, N. Gisin, M. Nilsson, S. Kröll, and J. I. Cirac, Quantum memory for nonstationary light fields based on controlled reversible inhomogeneous broadening, Phys. Rev. A **73**, 020302 (2006).

[12] E. Saglamyurek, T. Hrushevskyi, A. Rastogi, K. Heshami, and L. J. LeBlanc, Coherent storage and manipulation of broadband photons via dynamically controlled Autler-Townes splitting, Nat. Photonics **12**, 774 (2018).

[13] M. P. Hedges, J. J. Longdell, Y. Li, and M. J. Sellars, Efficient quantum memory for light, Nature **465**, 1052 (2010).

[14] K. Heshami, C. Santori, B. Khanaliloo, C. Healey, V. M. Acosta, P. E. Barclay, and C. Simon, Raman quantum memory based on an ensemble of nitrogen-vacancy centers coupled to a microcavity, Phys. Rev. A **89**, 040301 (2014).

[15] J. Guo, X. Feng, P. Yang, Z. Yu, L. Chen, C.-H. Yuan, and W. Zhang, High-performance Raman quantum memory with optimal control in room temperature atoms, Nat. Commun. **10**, 1 (2019).

[16] O. Katz and O. Firstenberg, Light storage for one second in room-temperature alkali vapor, Nat. Commun. **9**, 1 (2018).

[17] R. Zhang, S. R. Garner, and L. V. Hau, Creation of Long-Term Coherent Optical Memory via Controlled Nonlinear Interactions in Bose-Einstein Condensates, Phys. Rev. Lett. **103**, 233602 (2009).

[18] E. Saglamyurek, T. Hrushevskyi, A. Rastogi, L. W. Cooke, B. D. Smith, and L. J. LeBlanc, Storing short single-photon-level optical pulses in Bose–Einstein condensates

for high-performance quantum memory, New J. Phys. **23**, 043028 (2021).
[19] N. Lauk, N. Sinclair, S. Barzanjeh, J. P. Covey, M. Saffman, M. Spiropulu, and C. Simon, Perspectives on quantum transduction, Quantum Sci. Technol. **5**, 020501 (2020).
[20] L. M. Vandersypen and M. A. Eriksson, Quantum computing with semiconductor spins, Phys. Today **72**, 38 (2019).
[21] X. Xue, M. Russ, N. Samkharadze, B. Undseth, A. Sammak, G. Scappucci, and L. M. Vandersypen, Quantum logic with spin qubits crossing the surface code threshold, Nature **601**, 343 (2022).
[22] H. T. Tu, K. Y. Liao, Z. X. Zhang, X. H. Liu, S. Y. Zheng, S. Z. Yang, X. D. Zhang, H. Yan, and S. L. Zhu, High-efficiency coherent microwave-to-optics conversion via off-resonant scattering, Nat. Photonics **16**, 291 (2022).
[23] A. P. Higginbotham, P. Burns, M. Urmey, R. Peterson, N. Kampel, B. Brubaker, G. Smith, K. Lehnert, and C. Regal, Harnessing electro-optic correlations in an efficient mechanical converter, Nat. Phys. **14**, 1038 (2018).
[24] L. Fan, C.-L. Zou, R. Cheng, X. Guo, X. Han, Z. Gong, S. Wang, and H. X. Tang, Superconducting cavity electro-optics: A platform for coherent photon conversion between superconducting and photonic circuits, Sci. Adv. **4**, eaar4994 (2018).
[25] T. Vogt, C. Gross, J. Han, S. B. Pal, M. Lam, M. Kiffner, and W. Li, Efficient microwave-to-optical conversion using Rydberg atoms, Phys. Rev. A **99**, 023832 (2019).
[26] L. A. Williamson, Y.-H. Chen, and J. J. Longdell, Magneto-optic Modulator with Unit Quantum Efficiency, Phys. Rev. Lett. **113**, 203601 (2014).
[27] F. K. Asadi, J.-W. Ji, and C. Simon, Proposal for transduction between microwave and optical photons using ^{167}Er-doped yttrium orthosilicate, Phys. Rev. A **105**, 062608 (2022).
[28] C. O'Brien, N. Lauk, S. Blum, G. Morigi, and M. Fleischhauer, Interfacing Superconducting Qubits and Telecom Photons via a Rare-Earth-Doped Crystal, Phys. Rev. Lett. **113**, 063603 (2014).
[29] B. Li, P.-B. Li, Y. Zhou, S.-L. Ma, and F.-L. Li, Quantum microwave-optical interface with nitrogen-vacancy centers in diamond, Phys. Rev. A **96**, 032342 (2017).
[30] X. Fernandez-Gonzalvo, Y.-H. Chen, C. Yin, S. Rogge, and J. J. Longdell, Coherent frequency up-conversion of microwaves to the optical telecommunications band in an Er:YSO crystal, Phys. Rev. A **92**, 062313 (2015).
[31] M. Soltani, M. Zhang, C. Ryan, G. J. Ribeill, C. Wang, and M. Loncar, Efficient quantum microwave-to-optical conversion using electro-optic nanophotonic coupled resonators, Phys. Rev. A **96**, 043808 (2017).
[32] K. Stannigel, P. Rabl, A. S. Sørensen, P. Zoller, and M. D. Lukin, Optomechanical Transducers for Long-Distance Quantum Communication, Phys. Rev. Lett. **105**, 220501 (2010).
[33] R. Hisatomi, A. Osada, Y. Tabuchi, T. Ishikawa, A. Noguchi, R. Yamazaki, K. Usami, and Y. Nakamura, Bidirectional conversion between microwave and light via ferromagnetic magnons, Phys. Rev. B **93**, 174427 (2016).
[34] S. Das, V. E. Elfving, S. Faez, and A. S. Sørensen, Interfacing Superconducting Qubits and Single Optical Photons using Molecules in Waveguides, Phys. Rev. Lett. **118**, 140501 (2017).
[35] T. Xie, J. Rochman, J. G. Bartholomew, A. Ruskuc, J. M. Kindem, I. Craiciu, C. W. Thiel, R. L. Cone, and A. Faraon, Characterization of Er^{3+}:YV O4 for microwave to optical transduction, Phys. Rev. B **104**, 054111 (2021).
[36] L. Bergeron, C. Chartrand, A. T. K. Kurkjian, K. J. Morse, H. Riemann, N. V. Abrosimov, P. Becker, H.-J. Pohl, M. L. W. Thewalt, and S. Simmons, Silicon-Integrated Telecommunications Photon-Spin Interface, PRX Quantum **1**, 020301 (2020).
[37] D. B. Higginbottom, *et al.*, Optical observation of single spins in silicon, Nature **607**, 266 (2022).
[38] D. I. D. Cho, S. Hong, M. Lee, and T. Kim, A review of silicon microfabricated ion traps for quantum information processing, Micro Nano Syst. Lett. **3**, 2 (2015).
[39] M. Veldhorst, H. G. Eenink, C. H. Yang, and A. S. Dzurak, Silicon CMOS architecture for a spin-based quantum computer, Nat. Commun. **8**, 1 (2017).
[40] F. Arute, *et al.*, Quantum supremacy using a programmable superconducting processor, Nature **574**, 505 (2019).
[41] J. J. Pla, K. Y. Tan, J. P. Dehollain, W. H. Lim, J. J. L. Morton, D. N. Jamieson, A. S. Dzurak, and A. Morello, A single-atom electron spin qubit in silicon, Nature **489**, 541 (2012).
[42] J. Wang, F. Sciarrino, A. Laing, and M. G. Thompson, Integrated photonic quantum technologies, Nat. Photonics **14**, 273 (2020).
[43] E. Irion, N. Burger, K. Thonke, and R. Sauer, The defect luminescence spectrum at 0.9351 eV in carbon-doped heat-treated or irradiated silicon, **18**, 5069 (1985).
[44] A. N. Safonov, E. C. Lightowlers, G. Davies, P. Leary, R. Jones, and S. Öberg, Interstitial-Carbon Hydrogen Interaction in Silicon, Phys. Rev. Lett. **77**, 4812 (1996).
[45] E. R. MacQuarrie, C. Chartrand, D. B. Higginbottom, K. J. Morse, V. A. Karasyuk, S. Roorda, and S. Simmons, Generating T centres in photonic silicon-on-insulator material by ion implantation, New J. Phys. **23**, 103008 (2021).
[46] A. DeAbreu, C. Bowness, A. Alizadeh, C. Chartrand, N. A. Brunelle, E. R. Macquarrie, N. R. Lee-Hone, M. Ruether, M. Kazemi, A. T. K. Kurkjian, S. Roorda, N. V. Abrosimov, H.-J. Pohl, M. L. W. Thewalt, D. B. Higginbottom, and S. Simmons, Waveguide-integrated silicon T centres, ArXiv:2209.14260v1 (2022).
[47] D. Dhaliah, Y. Xiong, A. Sipahigil, S. M. Griffin, and G. Hautier, First-principles study of the T center in silicon, Phys. Rev. Mater. **6**, L053201 (2022).
[48] R. C. Hilborn, Einstein coefficients, cross sections, f values, dipole moments, and all that, Am. J. Phys. **50**, 982 (1982).
[49] K. Murata, Y. Yasutake, K. I. Nittoh, S. Fukatsu, and K. Miki, High-density G-centers, light-emitting point defects in silicon crystal, AIP Adv. **1**, 032125 (2011).
[50] E. Rotem, J. M. Shainline, and J. M. Xu, Enhanced photoluminescence from nanopatterned carbon-rich silicon grown by solid-phase epitaxy, Appl. Phys. Lett. **91**, 051127 (2007).
[51] M. A. Green, Self-consistent optical parameters of intrinsic silicon at 300 K including temperature coefficients, **92**, 1305 (2008).
[52] A. Markosyan, A. E. Shitikov, I. A. Bilenko, M. L. Gorodetsky, N. M. Kondratiev, and V. E. Lobanov, Billion Q-factor in silicon WGM resonators, Optica **5**, 1525 (2018).

[53] T. Asano, Y. Ochi, Y. Takahashi, K. Kishimoto, and S. Noda, Photonic crystal nanocavity with a Q factor exceeding eleven million, Opt. Express **25**, 1769 (2017).
[54] E. Arimondo and G. Orriols, Nonabsorbing atomic coherences by coherent two-photon transitions in a three-level optical pumping, Lett. Nuovo Cimento Ser. 2 **17**, 333 (1976).
[55] H. R. Gray, R. M. Whitley, and C. R. Stroud, Coherent trapping of atomic populations, Opt. Lett. **3**, 218 (1978).
[56] K.-J. Boller, A. Imamoğlu, and S. E. Harris, Observation of Electromagnetically Induced Transparency, Phys. Rev. Lett. **66**, 2593 (1991).
[57] G. Alzetta, A. Gozzini, L. Moi, and G. Orriols, An experimental method for the observation of r.f. transitions and laser beat resonances in oriented Na vapour, Nuovo Cimento B Ser. 11 **36**, 5 (1976).
[58] R. Rakhmatullin, E. Hoffmann, G. Jeschke, and A. Schweiger, Dark magnetic resonance in an electron-nuclear spin system, Phys. Rev. A: At., Mol., Opt. Phys. **57**, 3775 (1998).
[59] C. Wei and N. B. Manson, Observation of electromagnetically induced transparency within an electron spin resonance transition, J. Opt. B: Quantum Semiclass. Opt. **1**, 464 (1999).
[60] L. Childress and J. McIntyre, Multifrequency spin resonance in diamond, Phys. Rev. A: At., Mol., Opt. Phys. **82**, 033839 (2010).
[61] S. Novikov, T. Sweeney, J. E. Robinson, S. P. Premaratne, B. Suri, F. C. Wellstood, and B. S. Palmer, Raman coherence in a circuit quantum electrodynamics lambda system, Nat. Phys. **12**, 75 (2015).
[62] P. Jamonneau, G. Hétet, A. Dréau, J. F. Roch, and V. Jacques, Coherent Population Trapping of a Single Nuclear Spin under Ambient Conditions, Phys. Rev. Lett. **116**, 043603 (2016).
[63] M. Lukin, Colloquium: Trapping and manipulating photon states in atomic ensembles, Rev. Mod. Phys. **75**, 457 (2003).
[64] K. Reim, J. Nunn, V. Lorenz, B. Sussman, K. Lee, N. Langford, D. Jaksch, and I. Walmsley, Towards high-speed optical quantum memories, Nat. Photonics **4**, 218 (2010).
[65] Y. F. Hsiao, P. J. Tsai, H. S. Chen, S. X. Lin, C. C. Hung, C. H. Lee, Y. H. Chen, Y. F. Chen, I. A. Yu, and Y. C. Chen, Highly Efficient Coherent Optical Memory Based on Electromagnetically Induced Transparency, Phys. Rev. Lett. **120**, 183602 (2018).
[66] M. Hosseini, G. Campbell, B. M. Sparkes, P. K. Lam, and B. C. Buchler, Unconditional room-temperature quantum memory, Nat. Phys. **7**, 794 (2011).
[67] Y.-W. Cho, G. T. Campbell, J. L. Everett, J. Bernu, D. B. Higginbottom, M. T. Cao, J. Geng, N. P. Robins, P. K. Lam, and B. C. Buchler, Highly efficient optical quantum memory with long coherence time in cold atoms, Optica **3**, 100 (2016).
[68] A. V. Gorshkov, A. André, M. D. Lukin, and A. S. Sørensen, Photon storage in λ-type optically dense atomic media. III. Effects of inhomogeneous broadening, Phys. Rev. A **76**, 033806 (2007).
[69] Y.-C. Wei, B.-H. Wu, Y.-F. Hsiao, P.-J. Tsai, and Y.-C. Chen, Broadband coherent optical memory based on electromagnetically induced transparency, Phys. Rev. A **102**, 063720 (2020).
[70] A. Rastogi, E. Saglamyurek, T. Hrushevskyi, S. Hubele, and L. J. LeBlanc, Discerning quantum memories based on electromagnetically-induced-transparency and Autler-Townes-splitting protocols, Phys. Rev. A **100**, 012314 (2019).
[71] A. V. Gorshkov, A. André, M. D. Lukin, and A. S. Sørensen, Photon storage in λ-type optically dense atomic media. II. Free-space model, Phys. Rev. A **76**, 033805 (2007).
[72] I. Novikova, A. V. Gorshkov, D. F. Phillips, A. S. Sørensen, M. D. Lukin, and R. L. Walsworth, Optimal Control of Light Pulse Storage and Retrieval, Phys. Rev. Lett. **98**, 243602 (2007).
[73] I. Novikova, N. B. Phillips, and A. V. Gorshkov, Optimal light storage with full pulse-shape control, Phys. Rev. A **78**, 021802 (2008).
[74] N. B. Phillips, A. V. Gorshkov, and I. Novikova, Optimal light storage in atomic vapor, Phys. Rev. A **78**, 023801 (2008).
[75] N. Lauk, C. O'Brien, and M. Fleischhauer, Fidelity of photon propagation in electromagnetically induced transparency in the presence of four-wave mixing, Phys. Rev. A **88**, 013823 (2013).
[76] A. V. Gorshkov, A. André, M. D. Lukin, and A. S. Sørensen, Photon storage in λ-type optically dense atomic media. I. Cavity model, Phys. Rev. A **76**, 033804 (2007).
[77] A. V. Gorshkov, A. André, M. Fleischhauer, A. S. Sørensen, and M. D. Lukin, Universal Approach to Optimal Photon Storage in Atomic Media, Phys. Rev. Lett. **98**, 123601 (2007).
[78] K. Heshami, A. Green, Y. Han, A. Rispe, E. Saglamyurek, N. Sinclair, W. Tittel, and C. Simon, Controllable-dipole quantum memory, Phys. Rev. A **86**, 013813 (2012).
[79] L. Ma, X. Lei, J. Yan, R. Li, T. Chai, Z. Yan, X. Jia, C. Xie, and K. Peng, High-performance cavity-enhanced quantum memory with warm atomic cell, Nat. Commun. **13**, 1 (2022).
[80] L. Heller, P. Farrera, G. Heinze, and H. De Riedmatten, Cold-Atom Temporally Multiplexed Quantum Memory with Cavity-Enhanced Noise Suppression, Phys. Rev. Lett. **124**, 210504 (2020).
[81] J.-W. Ji, Y.-F. Wu, S. C. Wein, F. K. Asadi, R. Ghobadi, and C. Simon, Proposal for room-temperature quantum repeaters with nitrogen-vacancy centers and optomechanics, Quantum **6**, 669 (2022).
[82] N. Sangouard, C. Simon, J. Minář, H. Zbinden, H. De Riedmatten, and N. Gisin, Long-distance entanglement distribution with single-photon sources, Phys. Rev. A **76**, 050301 (2007).
[83] Y. Wu, J. Liu, and C. Simon, Near-term performance of quantum repeaters with imperfect ensemble-based quantum memories, Phys. Rev. A **101**, 042301 (2020).
[84] N. Sinclair, E. Saglamyurek, H. Mallahzadeh, J. A. Slater, M. George, R. Ricken, M. P. Hedges, D. Oblak, C. Simon, and W. Sohler, *et al.*, Spectral Multiplexing for Scalable Quantum Photonics Using an Atomic Frequency Comb Quantum Memory and Feed-Forward Control, Phys. Rev. Lett. **113**, 053603 (2014).